Indonesian Journal of Electronics, Electromedical Engineering, and Medical Informatics e-ISSN: 2656-8624
Homepage: https://ijeeemi.org/; Vol. 8, No. 3, pp. 431-440, August 2026

RESEARCH PAPER **OPEN ACCESS**

Image Quality of Decomposition Based on Near-Infrared Transmission Using The Gram-Schmidt Process

Toto Aminoto
Department of Physiotherapy, Politeknik Kesehatan Kemenkes Jakarta III, Jakarta, Indonesia

ABSTRACT The image decomposition process using near-infrared is influenced by the combination of wavelengths. Each material has selectivity at certain wavelengths. This selectivity affects the decomposition process. The results of the study show that the combination of using 3 wavelengths produces imperfect decomposition. One of the causes is that the attenuation value in the form of a matrix does not show orthogonal properties. The Gram-Schmidt process is used to make the column vectors orthogonal to each other. The purpose of this study is to measure the quality of the decomposed image using the Gram-Schmidt process. The indicators used to measure the quality are the CNR, SSIM, MSE, and PSNR values. The Lambert-Beer equation performs a natural logarithmic operation, producing a linear relationship between intensity level, attenuation coefficient, and thickness. By varying three different wavelengths and three different materials, three linear equations are obtained. The solution to these three linear equations can be expressed in the form of a 3x3 matrix. The rows represent the differences in attenuation coefficient values for the three materials at a single wavelength, while the columns represent the differences in attenuation coefficient values due to different wavelengths within the same material. This thickness value can be used to create an image reconstruction that can decompose the material's composition. The research results indicate that the decomposition of margarine and PVC occurs with the wavelength combination of 780 nm–830 nm–980 nm, whereas silicone rubber occurs with the combination of 780 nm–808 nm–980 nm. The quality of the resulting decomposed images is characterized by the lowest MSE and the highest PSNR and CNR values, while the SSIM values remain nearly identical. The Gram-Schmidt process is capable of enhancing the quality of the decomposed images.

Keyword: Short-chair; Transmittance image; tomography; image decomposition; attenuation-coefficient; matrix inverse; near-infrared

I. Introduction

Near-infrared-based imaging has been widely developed. Near-infrared light has a short wavelength of about 380 nm-1100 nm [1]. Near-infrared-based imaging has been widely developed. Near-infrared has optical properties, so if it passess through an object, interactions occur in the form of reflection, transmission, absorption, and refraction. Thus, near-infrared is able to carry information on the optical properties of the object. The advantages of near-infrared include having non-ionizing, non-invasive, and non-radiative properties [2-4]. The weakness of near-infrared is that if tomography is done, all components of the network will be captured in one image. This makes it difficult to diagnose a disease that only affects one particular tissue, such as a fractured bone. The hand contains numerous body tissues, such as skin, bones, muscles, and others. A tomography scan produces a single image composed of these tissues. To diagnose this, only the bone portion must be displayed. This requires separating the bone tissue from the other components to ensure a more accurate diagnosis.

Thus, it is necessary to develop a special method to decompose body tissue images. A near-infrared-based image decomposition technique using transmittance mode has been developed. One mode of transmittance is to use the Lambert-Beer equation [5]. With this equation, image decomposition can be performed based on the thickness function [6]. The decomposition method that has been developed is still basic in nature, so it does not address more complex problems. In the previous experiments, the image decomposition of the phantom material, which consisted of silicon rubber and margarine, was successfully carried out. In this study, the thickness of several components has been identified. Thus, the thickness of other components can easily be calculated and displayed in the form of an image. In the human body, there are several tissues, consisting of muscles, skin, and bones, whose thickness is not known with certainty. So it is necessary to develop an image decomposition method that can determine the thickness levels of a network, each of which is unknown. With these thicknesses, an image can be reconstructed.

The magnitude of the intensity value that passes through a material composed of several components, each of which varies in thickness, causes the output intensity to experience exponential attenuation according to the Lambert-Beer formulation. Based on this formulation, if infrared light with a certain wavelength is passed through several tissues, it will produce an attenuation coefficient value that varies depending on the constituent materials of the network. The relationship between intensity level, attenuation coefficient, and thickness can be expressed in a linear equation by performing natural logarithmic operations. By varying the 3 wavelengths and 3 different materials, 3 linear equations of the relationship will be obtained. Merging these 3 linear equations results in an equation in the matrix. By using the matrix equation, the thickness value of a particular network at a one-pixel point can be determined. The results of solving some of these linear

Manuscript received 9 March 2026; Revised 20 April 2026;; Accepted 15 June 2026; Available online 27 August 2026
DOI: https://doi.org/10.35882/ijeeemi.v8i3.335

equations produce a 3x3 attenuation coefficient matrix measuring 3x3. The row vector in the matrix represents the difference in the value of the attenuation coefficient of three different materials at one wavelength, while the column vector represents the difference in the value of the attenuation coefficient due to the difference in wavelength in the same material.

The attenuation coefficient matrix plays a crucial role in eliminating certain images during the decomposition process. The attenuation coefficient value depends not only on the material type but also on the wavelength. The combination of three different wavelengths significantly influences the matrix composition. The coefficient matrix value indicates the level of linear independence. To achieve the desired decomposition, linear independence plays a significant role, so the combination of wavelengths is crucial in determining the quality of the resulting image. Previous research has shown that separation between materials has not been perfect due to issues with the attenuation coefficient matrix determinant. The higher the determinant value, the better the separation. Therefore, a high-value coefficient matrix determinant is created; one way of maximizing linear independence is by creating a projection so that the column vectors are orthogonal and orthonormal. One of the reasons for suboptimal decomposition is the lack of orthogonality and orthonormality. This is because the wavelengths used are close together, resulting in attenuation coefficients that are also close in value

For this purpose, the attenuation coefficient matrix is projected using the Gram-Schmidt process. With this method, it is hoped that the image decomposition process will be better. Because the value of the attenuation coefficient depends on the wavelength, in this study the attenuation coefficient was first measured using 4 different wavelengths, namely 780 nm, 808 nm, 830 nm, and 980 nm. Of the 4 types of wavelengths, a combination of 3 types of wavelengths will be used in one decomposition process. Thus, there are four kinds of combination variations, namely 780 nm-808 nm-980 nm, 780 nm-830 nm-980 nm, 780 nm-808 nm-830 nm, and 808 nm-830 nm-980 nm. This study used a phantom consisting of silicone rubber, PVC, and margarine [7-10]. The use of phantoms is considered stable in calculating the attenuation coefficient value. The resulting decomposition image is considered satisfactory if it displays the image of a specific material while eliminating others. When displaying an image of PVC, images of silicone rubber and margarine are eliminated, and so on. The data acquisition process using near-infrared (NIR) is highly noisy. One such noise is salt-and-pepper noise. This noise significantly impacts the quality of the resulting image. Noise can reduce the information in the resulting image. Therefore, the decomposition process requires noise reduction. One technique for removing salt-and-pepper noise is using a median filter. The parameters used to indicate the level of image quality resulting from noise reduction are the MSE and PSNR values [11]. This study was limited to image decomposition methods for specific materials and did not address materials resembling human tissue. This is due to limited research literature.

In general, this study aims to analyze the quality of the decomposition image based on linearly independent properties by maximizing the determinant of the attenuation coefficient matrix using Schmidt's three-wavelength combination in the near-infrared spectrum of noise. The contribution of this research is to assist medical personnel in diagnosing diseases, particularly those involving medical imaging.

II. Materials and Method

A. Theoretical Development

In general, the attenuation equation can be stated in Beer-Lambert's law Eq. (1) [12-14]

$$\boldsymbol{I = I_0 e^{-\mu_\lambda d}} \quad (1)$$

where *Io* is the light intensity when it enters the material, *I* is the light intensity after passing through the material at thickness *d* and $\boldsymbol{\mu_\lambda}$ is the material attenuation coefficient, which is a function of wavelength. If the transmittance attenuation factor $\boldsymbol{T_\lambda}$ is the ratio of output to input intensity:

$$\boldsymbol{T_\lambda = \frac{I}{I_0} = e^{-\mu_\lambda d}} \quad (2)$$

Then Eq. (2) can be rewritten as Eq. (3):

$$\boldsymbol{\mu_\lambda = \frac{-ln\, T_\lambda}{d} = \frac{ln T_\lambda{}^{-1}}{d}} \quad (3)$$

Furthermore, if a near-infrared ray passes through a material composed of silicone rubber, margarine, and PVC with their respective thicknesses, then Eq. () can be described as follows:

$$\boldsymbol{T_\lambda = e^{-\mu_{s\lambda} d_s} . e^{-\mu_{m\lambda} d_m} . e^{-\mu_{p\lambda} d_p}} \quad (4)$$

where $\boldsymbol{\mu_{s\lambda}}$ represents Silicone Rubber attenuation coefficient at wavelength $\boldsymbol{\lambda}$, $\boldsymbol{\mu_{m\lambda}}$ represents Margarine attenuation coefficient at wavelength $\boldsymbol{\lambda}$, $\boldsymbol{\mu_{p\lambda}}$ PVC represents attenuation coefficient at wavelength $\boldsymbol{\lambda}$. Next Eq. (4) becomes a linear equation by carrying out the natural logarithmic transformation (*ln*) as follows [15, 16] :

$$\boldsymbol{ln\, T_\lambda = -[\mu_{s\lambda} d_s + \mu_{m\lambda} d_m + \mu_{p\lambda} d_p]} \quad (5)$$

Eq. (5) represents a linear equation for the coordinates of an image taken at a certain wavelength. To get the thickness value for each object at a certain point, 3 images are needed, each taken with 3 different wavelengths. Thus, there are 3 different linear equations.[17, 18]

$$\boldsymbol{\ln T_{\lambda 1} = -[\mu_{s\lambda 1} d_s + \mu_{m\lambda 1} d_m + \mu_{p\lambda 1} d_p]} \quad (6a)$$

$$\boldsymbol{\ln T_{\lambda 2} = -[\mu_{s\lambda 2} d_s + \mu_{m\lambda 2} d_m + \mu_{p\lambda 2} d_p]} \quad (6b)$$

$$\boldsymbol{\ln T_{\lambda 3} = -[\mu_{s\lambda 3} d_s + \mu_{m\lambda 3} d_m + \mu_{p\lambda 3} d_p]} \quad (6c)$$

where $\boldsymbol{\lambda_1}$, $\boldsymbol{\lambda_2}$ and $\boldsymbol{\lambda_3}$ represent different monochromatic wavelengths in the near-infrared spectrum. Furthermore, Eq.(6a) to (6c) above can be written in matrix form [19, 20]

$$-\begin{bmatrix} \ln T_{\lambda 1} \\ \ln T_{\lambda 2} \\ \ln T_{\lambda 3} \end{bmatrix} = \begin{bmatrix} \mu_{s\lambda 1} & \mu_{m\lambda 1} & \mu_{p\lambda 1} \\ \mu_{s\lambda 2} & \mu_{m\lambda 2} & \mu_{p\lambda 2} \\ \mu_{s\lambda 3} & \mu_{m\lambda 3} & \mu_{p\lambda 3} \end{bmatrix} \begin{bmatrix} d_s \\ d_m \\ d_p \end{bmatrix} \quad (7)$$

Manuscript received 9 March 2026; Revised 20 April 2026;; Accepted 15 June 2026; Available online 27 August 2026
DOI: https://doi.org/10.35882/ijeeemi.v8i3.335

So Eq. (7) in general can be simplified in the following form:

$$[\ln T_{\lambda m}^{-1}] = [\mu_{\lambda m}][dm] \quad m = 1,2,3 \tag{8}$$

where $[\mu_{\lambda m}]$ is the matrix attenuation coefficient. This $[\mu_{\lambda m}]$ matrix consists of 3 rows and 3 columns. Where the row states the results of measuring the attenuation coefficient of 3 different materials at the same wavelength, while the column measures the same material at 3 different wavelengths. Next, [dm] is the thickness vector of each material in the image coordinates. Meanwhile, $[\ln T_{\lambda m}^{-1}]$ is called the vector inverse natural logarithmic output to input ratio of the three images at those coordinates. $[\ln T_{\lambda m}^{-1}]$ vector is the ratio of input to output intensity, the result of the comparison of intensity measurements that pass through the material with no material. If the thickness is represented in the form of an image, then the higher value indicates the thickness of a layer of material at these coordinates. An image can be formed by compiling a matrix based on the thickness vector components corresponding to the layer at each point. The shape of the 2D matrix can be described as follows:

The transparency attenuation factor T_λ from the material measurement, if using a wavelength of 780 nm, is obtained by dividing the amount of intensity in the form of a line resulting from variations in thickness by the intensity of the reference line, following Eq. (3), which can be written as follows Eq. (9):

$$T_{780}(x,y) = \frac{I_{cm0.5@780}(x,y)}{I_{0@780}(x,y)} \tag{9}$$

and the attenuation coefficient value will be produced. As shown in Eq. (10):

$$\mu_{780}(x,y) = \frac{\ln(T_{cm0.5@780}(x,y))}{d_{cm}} \tag{10}$$

To predict the actual value of the attenuation coefficient, modeling is needed based on the measurement results of several different thicknesses. The results of the modeling used are nonlinear regression equations Eq. (11): [9, 21]

$$\mu_{i@\lambda} = \beta_0 + \beta_1 \frac{1}{d_i^3} \tag{11}$$

where d_i is the various material thicknesses, β_0 is the predicted asymptote value and β_1 is the material thickness coefficient. If you want to decompose an image of three materials, it takes the same three photos but uses three different monochromatic wavelengths. So the equation is listed in Eq. (12a) to Eq. (12c) [22]:

$$T_{\lambda 1}(x,y) = \frac{I_{\lambda 1}(x,y)}{I_{0@\lambda 1}(x,y)} \tag{12a}$$

$$T_{\lambda 2}(x,y) = \frac{I_{\lambda 2}(x,y)}{I_{0@\lambda 2}(x,y)} \tag{12b}$$

$$T_{\lambda 3}(x,y) = \frac{I_{\lambda 3}(x,y)}{I_{0@\lambda 3}(x,y)} \tag{12c}$$

Furthermore, for the attenuation coefficient matrix above to be operated, the matrix must meet the linear independent requirements [23, 24]. The condition is that if S=C_1, C_2, C_3 is a set of vectors in the attenuation coefficient matrix $[\mu_{\lambda m}]$, then the vector Eq. (13) is

$$k_1C_1 + k_2C_2 + k_3C_3 = 0 \tag{13}$$

The solution is (Eq. (14)):

$$k_1 = 0, k_2 = 0, k_3 = 0 \tag{14}$$

If the conditions in Eq. (9) and Eq. (10) are met, then the set S is called linearly independent in space $\boldsymbol{R}^3$, if it happens that one vector is a scalar multiple of the other vector, or if and only if the two vectors do not lie on the same line through the origin. The Gram-Schmidt process is one way to convert an arbitrary basis into both an orthogonal and an orthonormal basis. If the vectors $v_1 \ldots . v_n$. have a norm of 1 and are perpendicular to one another, the Gram-Schmidt process is as Eq. (15) to Eq. (18) [25-27]:

$$v_1 = u_1 \tag{15}$$

$$v_2 = u_2 - \frac{\langle u_2.v_1\rangle}{\|v_1\|^2} v_1 \tag{16}$$

$$v_3 = u_3 - \frac{\langle u_3.v_1\rangle}{\|v_1\|^2} v_1 - \frac{\langle u_3.v_2\rangle}{\|v_2\|^2} v_2 \tag{17}$$

$$v_4 = u_4 - \frac{\langle u_4.v_1\rangle}{\|v_1\|^2} v_1 - \frac{\langle u_4.v_2\rangle}{\|v_2\|^2} v_2 - \frac{\langle u_4.v_3\rangle}{\|v_3\|^2} v_3 \tag{18}$$

In general, noise will appear if the illuminating process imposes a condition of lighting intensity that is not perfect and uneven. In addition, the lack of camera sensitivity causes the processed signal to compete with the random quantum noise present in the detector device. Salt & pepper noise usually appears as black or white spots in the captured image, and the noise spreads randomly like salt and pepper over our breakfast, which has the density probability function characteristic [28, 29]. The probability density function for Salt & Pepper is explained in Eq. (19) :

$$P(z) = \begin{cases} P_a & if\ z = a \\ P_b & if\ z = b \\ 0 & otherwise \end{cases} \tag{19}$$

where P(z) is a probability noise function as a function of various kinds of wavelength dimensions, P_a is considered probability pepper (noise a), and P_b is considered probability salt (noise b). If b>a, it means the noise of intensity b will appear as a white spot, and the noise of intensity a will appear as a black spot. Unipolar is a condition in which impulse noise, apart from P_a or P_b, is valued at zero. An impulse noise value will appear as salt and pepper grain particles if the probability is more or less than zero and equally estimated. The median filter is categorized as a non-linear filter. The kernel in a median filter carries odd pixels placed pixel by pixel over the entire image area. Median filtering takes a certain area of the image according to a predetermined mask size and then looks at each pixel value in that area, and the middle value in the area is replaced with the median value (Eq. (20)) [30, 31]:

$$\hat{X}_{n,m} = med\{X'_{n',m'} : (n',m') \epsilon W(n,m)\} \tag{20}$$

$\hat{X}_{n,m}$ = Coordinate output median filter, med= operator median, $W(n,m)$= window size Filter median in coordinate (n, m) and value $w = 2r + 1$, where $r = 1, 2, \ldots$ SSIM (Structural Similarity Index) is a metric used to measure the similarity between two images based on human visual perception. SSIM compares structure, luminance, and contrast. SSIM values range from 0 to 1. The closer to 1, the more identical or highly similar the two images are. SSIM is calculated by combining three comparison components between the original image (x)

Manuscript received 9 March 2026; Revised 20 April 2026;; Accepted 15 June 2026; Available online 27 August 2026
DOI: https://doi.org/10.35882/ijeeemi.v8i3.335

and the test image (y):1.Luminance (I : Compares the average light intensity.2.Contrast (C): Compares the intensity distribution (standard deviation).3.Structure (s) :Compares the correlation between pixels after removing the effects of luminance and contrast Eq., (21) [32, 33]

$$SSIM(x,y) = \frac{2(\mu_x\mu_x+C_1)(2\sigma_{xy}+C_2)\mu}{(\mu_x^2+\mu_y^2+C_1)(\sigma_x^2+\sigma_y^2+C_2)} \quad (21)$$

where μ_x, μ_x are the average image intensity (luminance) x and y. σ_x^2, σ_y^2 *are* Image variance (contrast) x and y. σ_{xy} *is* Covariance between image x and y. C_1, C_2 are Stabilizing constant so that the divisor is not zero. Contrast-to-Noise Ratio (CNR**)** is a fundamental metric in imaging sciences used to quantify the ability to distinguish two regions of interest against the background of image noise (Eq. (22))

$$CNR = \frac{SI_x - SI_y}{SD_n} \quad (22)$$

SI_xSignal Intensity at ROI (Region of Interest) x. SI_y Signal Intensity at ROI (Region of Interest) y. SD_n Standard Deviation of Noise. Parameters to measure image quality are MSE and PSNR. The Mean Squared Error (MSE) is the average squared error value between the original image and the image repair results. Peak Signal Noise Ratio (PSNR) is a method that compares the maximum value of the measured signal with the amount of noise intensity in the signal Eq. (23) to Eq. (25) [11, 34, 35].

$$\boldsymbol{MSE = \frac{1}{MN}\sum_{i=1}^{M}\sum_{j=1}^{N}[f_{in}(x,y) - f_{out}(x,y)]^2} \quad (23)$$

$$\boldsymbol{a_{max} = \sum_{i=1}^{M}\sum_{j=1}^{N}[f(i,j)]} \quad (24)$$

$$\boldsymbol{PSNR = 20\, x \log 10\left(\frac{a_{max}}{\sqrt{MSE}}\right)} \quad \textbf{(25)}$$

In this study, the image capture method was carried out by transmittance, as shown in Fig. 1 below.

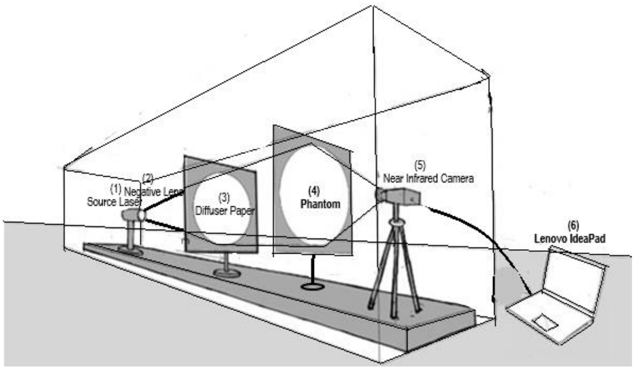

Fig.1. Experiment setup

B. Experimental Setup

The instrument used is the Lenovo IdeaPad 330 brand laptop. This laptop is useful for data processing and viewing the results of the decomposition of silicone rubber, PVC, and margarine materials. There are four lasers used, namely laser diodes at 780 nm, 120 mW, 808 nm, 300 mW, 830 nm, 300 mW, and 980 nm, 100 mW. There are two negative lenses, each with a focal point of 5 cm. The two lenses are mounted side by side. The purpose of this lens is to diverge the infrared light so that the diameter becomes wider. Near-infrared camera with Thorlabs CMOS CS505MU brand [36, 37]. The camera lens used is the MVL5M23. Useful for forming a field of view so that the image can be captured by the screen. Meanwhile, the diffuser paper is placed between the phantom and the camera. The diffuser paper is used to even out the spread of the light distribution. The materials used for this research are silicone rubber, PVC, and margarine. These materials vary in thickness from 0.4 cm, 0.5 cm, 0.6 cm, 0.7 cm, 0.8 cm, and 0.9 m.

III. Results

Before the decomposition process is carried out, the phantom constituent materials are first measured for their attenuation coefficient values. The thickness of all the materials to be measured varied from 0.4 cm, 0.5 cm, 0.6 cm, 0.7 cm, 0.8 cm, and 0.9 cm, respectively. Especially for margarine material packaged in a glass box. This thickness variation is to eliminate the reflectance mode. The thicker the material, the more dominant the transmittance mode is. With a reduced reflectance mode, the calculation of the attenuation coefficient is more valid. The first step is to measure the beam profile value of the material by varying the wavelength. In Fig. 2 below, there

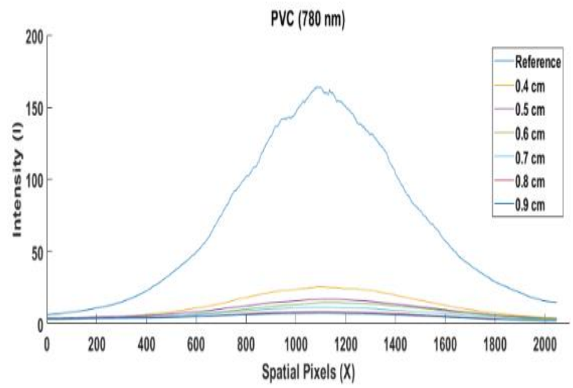

Fig. 2. Beam profile image PVC

is an example of the results of measuring the PVC beam profile at the 780-nm wavelength. This profile beam measurement varies with a thickness of 0.4 cm–0.9 cm and without PVC material. The profile beam without PVC

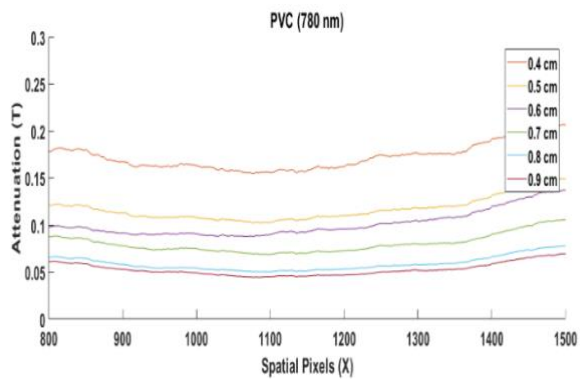

Fig. 3. The results of measuring the attenuation value of various thickness levels PVC

material is used as a reference image. When measuring 0.4 cm to 0.9 cm thick PVC material, the light intensity used is the same as when measuring the reference image. The near-infrared laser intensity output is set so that there is no saturation on the camera sensor. The

Manuscript received 9 March 2026; Revised 20 April 2026;; Accepted 15 June 2026; Available online 27 August 2026
DOI: https://doi.org/10.35882/ijeeemi.v8i3.335

intensity is taken in the form of a vertical line from the reference image. It can be seen that the beam profile of the reference image and the results of thickness variations are all close to the shape of the Gaussian distribution [38, 39]. One of the results of the Eq.9 calculation is a horizontal straight line, as shown in Fig. 3 As seen in Fig. 3, at any thickness, it shows a straight horizontal line. The level of straightness looks imperfect; this is due to various sources, such as noise. One of the causes of this noise is the uneven beam profile. For this reason, the horizontal line in Fig. 3 is carried by a moving average, then divided by the thickness of the material, and the attenuation coefficient value will be produced. Based on Eq. 10, the PVC attenuation coefficient at the wavelength of 780 nm was obtained for each of 0.4 cm, 0.5 cm, 0.6 cm, 0.7 cm, 0.8 cm, and 0.9 cm. At this thickness level, the attenuation coefficient measurement results show different values. To predict the actual value of the attenuation coefficient, modeling is needed based on the measurement results of several different thicknesses. Based on Eq. 11, the results of the non-linear regression of PVC are Eq. (25) [21, 40]

$$\boldsymbol{\mu_{i@\lambda} = 0.073 + 3.328\frac{1}{d_i^3}} \tag{25}$$

It can be seen from the measurement results that the thicker the material, the higher the attenuation coefficient, which leads to a certain stable value. So the value of the attenuation coefficient is taken as the asymptote value. Apart from PVC material, characterization was also carried out on several other materials, namely margarine and silicone rubber, by varying four different monochromatic wavelengths. By using the same method as described above, the attenuation coefficient of each type of material at certain wavelengths is obtained. The results of calculating the value of the attenuation coefficient can be written into a matrix as follows:
for 780nm, silicone rubber is 1.89, Margarine is 3.88, and PVC is 3.33. for 808nm, silicone rubber is 1.81, Margarine is 3.64, and PVC is 3.15 for 830nm silicone rubber is 1.40, Margarine is 2.99, and PVC is 2.85 for 980nm silicone rubber is 1.31, Margarine is 2.83, and PVC is 2.66

In this study, phantom decomposition was performed using combinations of three different wavelengths. This approach was adopted because three material variations were involved, while four wavelengths were available for use; the specific wavelengths were selected due to their ready availability on the market. Consequently, by combining three wavelengths out of the four available, four distinct attenuation coefficient matrices were generated. The determinant values for the wavelength combinations were as follows: 0.0192 for 780 nm–808 nm–980 nm; 0.0246 for 780 nm–808 nm–830 nm; 0.0484 for 780 nm–830 nm–980 nm; and 0.0492 for 808 nm–830 nm–980 nm. The phantom is composed of silicone rubber, margarine, and PVC, with the following composition. The total thickness of the phantom is 1.4 cm. Specifically, the total thickness of the silicone rubber component is 0.7 cm; this consists of two layers of silicone rubber, each 0.3 cm thick, and another layer that is 0.1 cm thick. The 0.1 cm thick silicone rubber layer features cutouts arranged according to the phantom's specific pattern. This 0.1 cm layer is positioned between the two 0.3 cm thick silicone rubber layers, and the cutouts within it are filled with margarine. Finally, a 0.7 cm thick PVC layer is placed at the bottom.

A. Margarine decomposition

Margarine Decomposition on the Phantom of Figure 5(a) is positioned between the laser and the camera, as shown in Fig. 1. This acquisition produces an image (I). If the

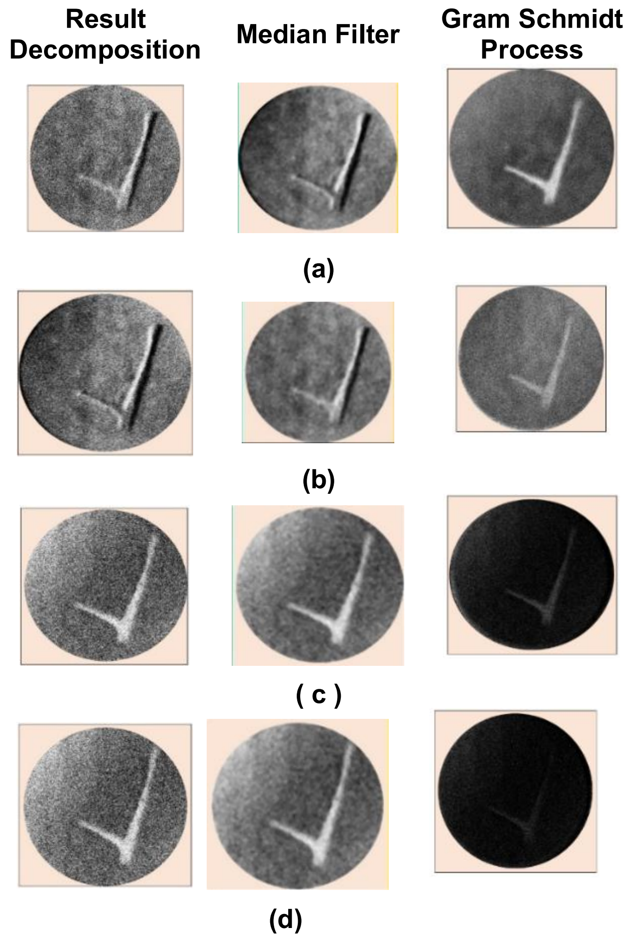

Fig 4. Results of image decomposition with various wavelength variations, (a) 780 nm-808nm-980 nm, (b) 780 nm-808 nm-830 nm, (c)780 nm-830 nm-980 nm, and (d) 808 nm-830nm-980nm (coloumn left) results decomposition Margarine (Coloumn Middle) Median Filter (Coloumn Right) Grap Schmidt Process

phantom is released, it will produce a reference image (Io). This acquisition process is carried out four times, according to the number of laser wavelengths. Then, the results of the decomposition of margarine material according to Equation 8 are shown in Fig. 4 below. The left column is the result of the decomposition of margarine material with other materials.

This decomposition is done with a combination of three different wavelengths. The middle column is the result of the image margarine decomposition after being given a median filter with a 7x7 kernel matrix. The rightmost column is the result of the decomposition using the Gram-Schmidt process. Fig. 4 above shows that by using the Gram-Schmidt process, the margarine material is clearly visible with the 780–808–980 nm wavelength combination compared to the other combinations; the margarine

Manuscript received 9 March 2026; Revised 20 April 2026;; Accepted 15 June 2026; Available online 27 August 2026
DOI: https://doi.org/10.35882/ijeeemi.v8i3.335

Indonesian Journal of Electronics, Electromedical Engineering, and Medical Informatics e-ISSN: 2656-8624
Homepage: https://ijeeemi.org/; Vol. 8, No. 3, pp. 431-440, August 2026

appears with high contrast. In contrast, the margarine material is not visible at all with the 808–830–980 nm combination. However, the opposite occurs when using a median filter: the latter combination yields a clearer view

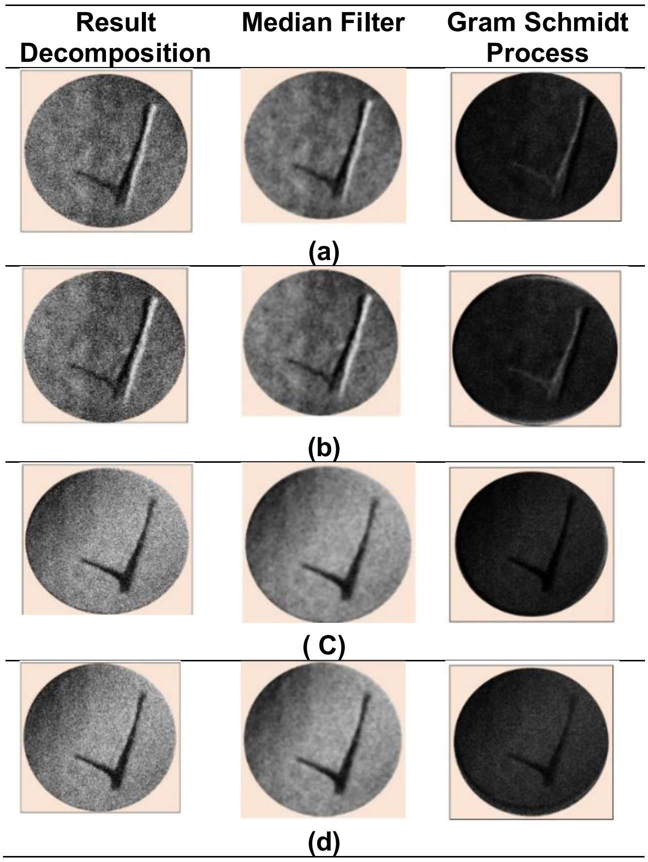

Fig. 5. (a) 780 nm-808nm-980 nm, (b) 780 nm-808 nm-830 nm, (c)780 nm-830 nm-980 nm, and (d) 808 nm-830nm-980nm (coloumn left) results decomposition Silicone Rubber (Coloumn Middle) Median Filter (Coloumn Right) Grap Schmidt Process

than the first.

Calculation results for MSE, CNR, PSNR and SSIM for the Silicone Rubber material for 780 nm-808nm-980 nm, value MSE is 24.20, PSNR is 34.33, CNR is 6.504, and SSIM is 0.998. For 780 nm-808 nm-830 nm, MSE is 21.62, PSNR is 34.91, CNR is 8.952, and SSIM is 0.998, For 780 nm-830 nm-980 nm, MSE is 19.09, PSNR is 35.36, CNR is 15.34, and SSIM is 0.998. For 808 nm-830nm-980nm MSE is 19.31, PSNR is 35.31, CNR is 14.447, and SSIM is 0.998. There are significant differences in the CNR, MSE, and PSNR values, whereas the SSIM values tend to be similar.

B. Silicone Rubber Decomposition

The decomposition results of the silicone rubber material according to Eq. 8 are shown in Fig. 5 below. The left column is the result of the decomposition of silicone rubber material with other materials. Calculation results for MSE, CNR, PSNR and SSIM material Silicone Rubber for 780 nm-808nm-980 nm, value MSE is 18.46, PSNR is 35.49, CNR is 6.69, and SSIM is 0.999. For 780 nm-808 nm-830 nm, MSE is 19.75, PSNR is 35.21, CNR is 3.314, and SSIM is 0.998. For 780 nm-830 nm-980 nm, MSE is 28.76, PSNR is 33.58, CNR is 6.464, and SSIM is 0.996. For 808 nm-830nm-980nm MSE is 28.80, PSNR is 33.57, CNR is 4.618, and SSIM is 0.997.

C. PVC Decomposition

The results of the decomposition of PVC material according to Eq. 8 are shown in Fig. 6 below. The left

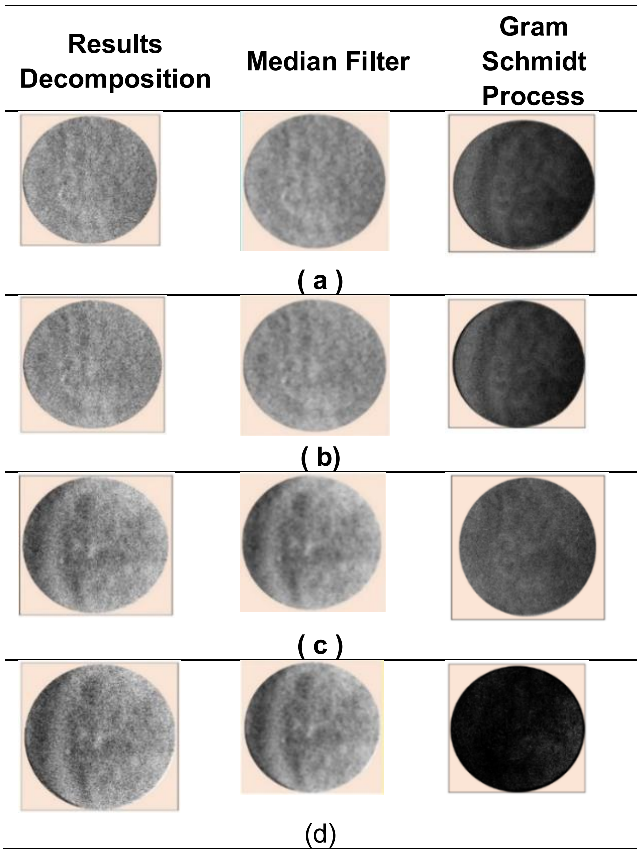

Fig.6. (a) 780 nm-808nm-980 nm, (b) 780 nm-808 nm-830 nm, (c)780 nm-830 nm-980 nm, and (d) 808 nm- (coloumn left) results decomposition PVC (Coloumn Middle) Median Filter (Coloumn Right) Grap Schmidt Process

column is the result of the decomposition of PVC material with other materials. Calculation results for MSE and PSNR for Silicone Rubber material for 780 nm-808nm-980 nm: the value of MSE is 49.94, PSNR is 31.18, CNR is 9.773, and SSIM is 0.997. For780 nm-808 nm-830 nm, MSE is 49.66, PSNR is 31.20, CNR is 4.779, and SSIM is 0.998. For 780 nm-830 nm-980 nm, MSE is 29.54, PSNR is 33.46, CNR is 1.068, and SSIM is 0.998. For 808 nm-830nm-980nm MSE is 32.06, PSNR is 33.11, CNR is 7.394, and SSIM is 0.998

IV. Discussion

The results of the calculation of the attenuation coefficient matrix $[\ln T_\lambda^{-1}]$ produce a determinant value that is not equal to zero, or $det[\ln T_\lambda^{-1}] \neq 0$ [41]. Thus, the combination is linearly independent. The matrix is invertible, so it can be used for the image decomposition

Manuscript received 9 March 2026; Revised 20 April 2026;; Accepted 15 June 2026; Available online 27 August 2026
DOI: https://doi.org/10.35882/ijeeemi.v8i3.335

process to get the $[\ln T_{\lambda}^{-1}]$ vector. Researchers have conducted studies on the decomposition process. Table 1 are studies related to decomposition. The following are studies related to decomposition. Some researchers have used the dorsum of the hand as a medium but were only able to isolate a single image specifically of blood vessels without successfully distinguishing other structures, despite the hand's complex composition of muscle, skin, and other tissues. Furthermore, the near-infrared lasers employed in these studies utilized only a single wavelength. In contrast, other research has successfully differentiated the constituent components of phantoms such as skin, flesh, and bone, though a limitation in the present study is the restricted availability of near-infrared laser wavelengths on the market [6]. This study refines the decomposition process using the Gram-Schmidt process

Table 1. Previous researchers regarding decomposition

Authors, year	Method	Limitations	Output
Christof Kauba , Bernhard Prommegger, [42]	*Circular Gabor Filter*	capable of separating a single image	displays only images of veins
Yiding Wang, Heng Cao, Xiaochen Jiang and Yuanyan Tang, [43]	Teksture blok	capable of separating a single image	displays only images of veins
Bogdan Belean, Mihaela Streza, Septimiu Crisan, Simina Emerich,[44]	Canny	capable of separating a single image	displays only images of veins
Ren Yu Lai, Kim Gaik Tay [45]	*Convolutional Neural Network-based (CNN)*	capable of separating a single image	displays only images of veins
Purnomo sidi priambodo [6]	*Invers matrik*	The near-infrared lasers used are limited.	displaying images of chicken bones, meat, and skin

in the decomposition of margarine.The results show that the combination of wavelengths 780 nm-830 nm-980 nm and 808 nm-830 nm-980 nm is closer to perfection. Because other materials, namely silicone rubber and PVC, were eliminated. The material that is eliminated is black, while the material that appears is white. The results of the median filter are also able to remove salt & pepper noise. Furthermore, by using the Gram-Schmidt process, the decomposition results are better because other materials look more black. Based on the calculation of the MSE and PSNR values, it shows that the wavelengths of 780 nm, 830 nm, and 980 nm are better because the MSE value is smaller and the PSNR is higher. Besides that, the CNR value is also the highest. Meanwhile, the SSIM values are almost the same in the decomposition of silicone rubber. The results show that the combination of wavelengths 780 nm-808 nm-980 nm and 780 nm-808 nm-830 nm is closer to perfection. Because other materials, namely margarine and PVC, were eliminated, Silicone rubber still has a thickness of about 0.6 cm in the area where there is margarine, so the image results look almost the same as the surroundings. Compared to the other wavelength combinations, it looks black. Furthermore, by using the Gram-Schmidt process, the decomposition results are better because other materials look more black. Based on the calculation of the MSE and PSNR values, it shows that the wavelengths of 780 nm, 808nm and 980 nm are better because the MSE value is smaller and the PSNR is the highest. The highest CNR and SSIM values.

in the decomposition of PVC. The results show that the combination of wavelengths 780 nm-830 nm-980 nm and 808 nm-830 nm-980 nm is closer to perfection. Because other materials, namely margarine and silicone rubber, were eliminated. Furthermore, by using the Gram-Schmidt process, the decomposition results are even more perfect because other materials are not visible. Based on the calculation of the MSE and PSNR values, it shows that the wavelengths of 780 nm, 830 nm, and 980 nm are better because the MSE value is smaller and the PSNR is the highest. The highest CNR value and SSIM approaching 1. The results show that the combination of the use of wavelengths of each material produces different decomposition processes due to the influence of the selective effect of absorption of photon energy by specific chemical bonds in the material. The limitation of this research is the use of only four types of wavelengths because the tools available on the market only have these wavelengths.

V. Conclusions

The phantom material decomposition process using the inverse matrix method was successfully carried out. In this study, the characteristics of linear independence were successfully demonstrated. One of its characteristics is that the magnitude of the determinant value of the attenuation coefficient matrix of the measurement results, which is not equal to zero. The results showed that the combination of wavelengths 780 nm, 830 nm, and 980 nm succeeded in decomposing margarine, with values MSE is 19.09, PSNR is 35.36, CNR is 15.34, and SSIM is 0.998. The results showed that the combination of wavelengths 780 nm, 808 nm, and 980 nm succeeded in decomposing silicone rubber with values MSE is 18.49, PSNR is 35.49, CNR is 6.89 and SSIM is 0.999 and The results showed that the combination of wavelengths 780 nm, 830 nm, and 980 nm succeeded in decomposing PVC with values MSE is 29.54, PSNR is 33.46, CNR is 10.07

Manuscript received 9 March 2026; Revised 20 April 2026;; Accepted 15 June 2026; Available online 27 August 2026
DOI: https://doi.org/10.35882/ijeeemi.v8i3.335

and SSIM is 0.998. Each material has characteristics for a certain combination of wavelengths. Image decomposition using the Gram-Schmidt process produces a more perfect elimination. This result can be seen with a more contrasting black color. Thus, the combination of using different wavelengths affects the quality level of the decomposed image. Besides that, the selection of the wavelength used should pay attention to the absorbance level of each material so that the selection of the variations will be more appropriate. For further research, it is necessary to use other methods as a more accurate determinant of the quality level of image decomposition. This study consisted of three materials and three different wavelengths. In the future, this research will show the amount of material and the number of laser wavelengths that are not the same.

Acknowledgment

The authors would like to thank the management and staff of the Universitas Indonesia optoelectronics laboratory Jakarta for their assistance during participant recruitment and data collection. The authors also thank all participants who voluntarily took part in this study.

Funding

The authors received no financial support for the research, authorship, and/or publication of this article.

Author Contributions

Toto Aminoto conceived and designed the study, coordinated the research activities, collected the data, and contributed to data analysis and interpretation. contributed to the study design, methodological supervision, and interpretation of the findings. Bedjo Utomo contributed to data analysis, literature review, and manuscript preparation. Isnanto contributed to data interpretation and critically revised the manuscript for important intellectual content. authors reviewed and approved the final manuscript and agreed to be accountable for all aspects of the work.

Data Availability

All data were obtained from experiments at the UI photonics laboratory.

Ethical Approval

No Ethical,.

Competing Interests

The authors declare that they have no financial or non-financial competing interests that could have influenced the conduct, analysis, interpretation, or reporting of this study.

References

[1]. Poon, J.K., et al., *Silicon photonics for the visible and near-infrared spectrum.* Advances in Optics and Photonics, 2024. **16**(1): p. 1-59. https://doi.org/10.1364/AOP.501846

[2]. Vitorino, R., et al., *Diagnostic and monitoring applications using near infrared (NIR) spectroscopy in cancer and other diseases.* Photodiagnosis and Photodynamic Therapy, 2023. **42**: p. 103633. https://doi.org/10.1016/j.pdpdt.2023.103633

[3]. Wu, S., et al., *Multiple defect‐induced high‐resolution near‐infrared mechanoluminescent materials for non‐destructive detection of blood glucose and lipids.* Advanced Materials, 2024. **36**(50): p. 2408508. https://doi.org/10.1002/adma.202408508Digital Object Identifier (DOI)

[4]. Zhang, S., et al., *Near-infrared luminescent materials: a review of their practical applications and prospective advancements.* Dalton Transactions, 2025. **54**(17): p. 6717-6740. https://doi.org/10.1039/D4DT03538K

[5]. Bozdoğan, A.E., *Polynomial equations based on bouguer–lambert and beer laws for deviations from linearity and absorption flattening.* Journal of Analytical Chemistry, 2022. **77**(11): p. 1426-1432. https://doi.org/10.1134/S1061934822110028

[6]. Priambodo, P.S., T. Aminoto, and B. Basari, *Decomposition Technique for Bio-Transmittance Imaging Based on Attenuation Coefficient Matrix Inverse.* Journal of Imaging, 2024. **10**(1): p. 22. https://doi.org/10.3390/jimaging10010022

[7]. Gu, F., et al., *Silicone rubber sealed channel induced self-healing of large bone defects: where is the limit of self-healing of bone?* Journal of Orthopaedic Translation, 2023. **43**: p. 21-35. https://doi.org/10.1016/j.jot.2023.09.001

[8]. Zhou, H., et al., *Nanosilica cross-linked polyurethane hybrid hydrogels to stabilize the silicone rubber based invasive electrode-neural tissue interface.* Colloids and Surfaces B: Biointerfaces, 2025. **251**: p. 114643. https://doi.org/10.1016/j.jot.2023.09.001

[9]. Aminoto, T., P.S. Priambodo, and H. Sudibyo, *Image Decomposition Technique Based on Near-Infrared Transmission.* Journal of Imaging, 2022. **8**(12): p. 322. https://doi.org/10.3390/jimaging8120322

[10]. Young, J., et al. *A low-cost PVC-based dual-modality kidney phantom*. in *Proceedings of SPIE--the International Society for Optical Engineering*. 2022. 10.1117/12.2611592

[11]. Al Najjar, Y., *Comparative analysis of image quality assessment metrics: MSE, PSNR, SSIM and FSIM.* International Journal of Science and Research (IJSR), 2024. **13**(3): p. 110-114. DOI: https: //orcid. org/0000 - 0002 - 3369 - 4999

[12]. Li, L., et al., *Study on the origin of linear deviation with the Beer-Lambert law in absorption spectroscopy by measuring sulfur dioxide.* Spectrochimica Acta Part A: Molecular and Biomolecular Spectroscopy, 2022. **275**: p. 121192. https://doi.org/10.1016/j.saa.2022.121192

[13]. Wadati, H., *Teaching light absorption and the Beer–Lambert law using everyday materials: a tomato juice experiment for introductory physics.* Physics

Manuscript received 9 March 2026; Revised 20 April 2026;; Accepted 15 June 2026; Available online 27 August 2026
DOI: https://doi.org/10.35882/ijeeemi.v8i3.335

Education, 2026. **61**(2): p. 025016. **DOI** 10.1088/1361-6552/ae3f71

[14]. Mallet, A., et al., *Relating near-infrared light path-length modifications to the water content of scattering media in near-infrared spectroscopy: toward a new Bouguer–Beer–Lambert law.* Analytical Chemistry, 2021. **93**(17): p. 6817-6823. **DOI** 10.1088/1361-6552/ae3f71

[15]. Blessner, D. *Alternative Modality of Delivery for the Exponential and Logarithmic Functions*. in *2023 Fall Mid Atlantic Conference: Meeting our students where they are and getting them where they need to be*. 2023. 10.18260/1-2--45114

[16]. Park, D., E. Lee, and J.-W. Lee. *Powerformer: Efficient and high-accuracy privacy-preserving language model with homomorphic encryption*. in *Proceedings of the 63rd Annual Meeting of the Association for Computational Linguistics (Volume 1: Long Papers)*. 2025. 10.18653/v1/2025.acl-long.543

[17]. Oshina, I. and J. Spigulis, *Beer–Lambert law for optical tissue diagnostics: current state of the art and the main limitations.* Journal of Biomedical Optics, 2021. **26**(10): p. 100901. https://doi.org/10.1117/1.JBO.26.10.100901

[18]. Spigulis, J., et al., *Smartphone snapshot mapping of skin chromophores under triple-wavelength laser illumination.* Journal Biomedical Optics, 2017. **22**(9): p. 091508. https://doi.org/10.1117/1.JBO.22.9.091508

[19]. Caridade, C. and V. Pereira. *Matrices In Motion: An Educational Journey Through The Universe Of Linear Algebra*. in *Inted2025 Proceedings*. 2025. IATED. doi: 10.21125/inted.2025.1635

[20]. Lestari, G., *Determinan Matrik 3x3 dengan Metode Doolittle.* Jurnal Pustaka Cendekia Pendidikan, 2024. **2**(1): p. 30-34. **DOI:** https://doi.org/10.70292/jpcp.v2i1.26

[21]. Zhou, W., Z. Yan, and L. Zhang, *A comparative study of 11 non-linear regression models highlighting autoencoder, DBN, and SVR, enhanced by SHAP importance analysis in soybean branching prediction.* Scientific Reports, 2024. **14**(1): p. 5905. https://doi.org/10.1038/s41598-024-55243-x

[22]. Ballester, M., et al., *Review and novel formulae for transmittance and reflectance of wedged thin films on absorbing substrates.* Measurement Science and Technology, 2025. **36**(2): p. 025502. **DOI** 10.1088/1361-6501/ada305

[23]. Chen, R.-M., *A Complete Characterization of Linear Dependence and Independence for All 4-by-4 Metric Matrices.* Axioms, 2024. **13**(9): p. 622. https://doi.org/10.3390/axioms13090622

[24]. Karunaratne, S. and A. Idamekorala, *55 Additions Suffice for 3x3 Matrix Multiplication at Rank 23.* arXiv preprint arXiv:2607.28676, 2026.
https://doi.org/10.48550/arXiv.2607.28676

[25]. Balabanov, O. and L. Grigori, *Randomized block–Schmidt process for the solution of linear systems and eigenvalue problems.* SIAM Journal on Scientific Computing, 2025. **47**(1): p. A553-A585. https://doi.org/10.1137/22M1518396

[26]. Okazaki, H., *On the formalization of Gram-Schmidt process for orthonormalizing a set of vectors.* Formalized Mathematics, 2023. **31**(1): p. 53-57. 10.2478/forma-2023-0005

[27]. Deng, Y., *On p-adic Gram–Schmidt Orthogonalization Process.* Frontiers of Mathematics, 2025. **20**(2): p. 299-311. https://doi.org/10.1007/s11464-023-0111-0

[28]. Azzeh, J., B. Zahran, and Z. Alqadi, *Salt and pepper noise: Effects and removal.* JOIV: International Journal on Informatics Visualization, 2018. **2**(4): p. 252-256. http://dx.doi.org/10.30630/joiv.2.4.151

[29]. Rafiee, A.A. and M. Farhang, *A deep convolutional neural network for salt-and-pepper noise removal using selective convolutional blocks.* Applied Soft Computing, 2023. **145**: p. 110535. https://doi.org/10.1016/j.asoc.2023.110535

[30]. Oboué, Y.A.S.I., et al., *An advanced median filter for improving the signal-to-noise ratio of seismological datasets.* Computers & Geosciences, 2024. **182**: p. 105464. https://doi.org/10.1016/j.cageo.2023.105464

[31]. Guan, S., et al., *Adaptive median filter salt and pepper noise suppression approach for common path coherent dispersion spectrometer.* Scientific Reports, 2024. **14**(1): p. 17445. https://doi.org/10.1038/s41598-024-66649-y

[32]. Raigonda, M.R., *Signature verification system using SSIM in image processing.* Journal of Scientific Research and Technology, 2024: p. 5-11. **DOI:** https://doi.org/10.61808/jsrt79

[33]. Martini, M. *A simple relationship between SSIM and PSNR for DCT-based compressed images and video: SSIM as content-aware PSNR*. in *2023 IEEE 25th International Workshop on Multimedia Signal Processing (MMSP)*. 2023. IEEE. 10.1109/MMSP59012.2023.10337706

[34]. Bruntha, P.M., et al., *Application of switching median filter with L 2 norm-based auto-tuning function for removing random valued impulse noise.* Aerospace systems, 2023. **6**(1): p. 53-59. https://doi.org/10.1007/s42401-022-00160-y

[35]. Khudhair, K.T., et al. *A novel medical image enhancement technique based on hybrid method*. in *Journal of Physics: Conference Series*. 2023. IOP Publishing. **DOI** 10.1088/1742-6596/2432/1/012021

[36]. Zhu, Q., et al., *Microwave Near Field Imaging of Externally Injected Signals in an Encapsulated Electronic Device.* Micromachines, 2026. **17**(6): p. 711. https://doi.org/10.3390/mi17060711

[37]. Lourens, D., et al., *Time-resolved single-shot imaging of ultrafast polarization dynamics in barium titanate using pump-probe second-harmonic generation microscopy.* Review of Scientific Instruments, 2025. **96**(7). https://doi.org/10.1063/5.0266905

[38]. Orekhov, A., L. Rabinskiy, and G. Fedotenkov, *Analytical model of heating an isotropic half-space*

Manuscript received 9 March 2026; Revised 20 April 2026;; Accepted 15 June 2026; Available online 27 August 2026
DOI: https://doi.org/10.35882/ijeeemi.v8i3.335

by a moving laser source with a Gaussian distribution. Symmetry, 2022. **14**(4): p. 650. https://doi.org/10.3390/sym14040650
[39]. Wu, Y.-K., et al., *Novel frequency control technologies for wind turbines based on modified gaussian curve settings.* IEEE Transactions on Industry Applications, 2025. 10.1109/TIA.2025.3540802
[40]. Bai, K., et al., *Recent advances in the combination of nonlinearity and exceptional points.* Applied Physics Reviews, 2026. **13**(2). https://doi.org/10.1063/5.0306393
[41]. Chetty, R., et al., *Social capital II: determinants of economic connectedness.* Nature, 2022. **608**(7921): p. 122-134. https://doi.org/10.1038/s41586-022-04997-3
[42]. Kauba, C., B. Prommegger, and A. Uhl, *OpenVein—An open-source modular multipurpose finger vein scanner design*, in *Handbook of vascular biometrics*. 2019, Springer International Publishing Cham. p. 77-111. 10.1007/978-3-030-27731-4
[43]. Wang, Y., et al., *Recognition of dorsal hand vein based bit planes and block mutual information.* Sensors, 2019. **19**(17): p. 3718. https://doi.org/10.3390/s19173718
[44]. Belean, B., et al., *Dorsal hand vein pattern analysis and neural networks for biometric authentication.* Studies in Informatics and Control, 2017. **26**(3): p. 305. https://doi.org/10.24846/v26i3y201706
[45]. Lai, R.Y., et al., *Dorsal hand vein authentication system using convolution neural network.* Int J Emerg Technol Adv Eng, 2022. **12**(8): p. 83-90. DOI: 10.46338/ijetae0822_11

Author Biography

Toto Aminoto received the B.S. degree in Physics with a concentration in Instrumentation Electronics from Gadjah Mada University in 2001, an M. Si. degrees in Physics with a concentration in theoretical Physics from Indonesia University, Indonesia, in 2006, and the Ph.D. degree in Electrical Engineering with a concentration in biomedical engineering from Indonesia University, Depok, Indonesia, in 2023. Joined as a lecturer since 2014.Since 2024, he has been an Assistant Professor with the Physiotherapy, Health Polytechnic, Ministry of Health, Jakarta **III**. His current research interests include image processing, electromedicine and physics. He is a reviewer for the journal Result of Engineering from Elsevier and currently teaching electrophysics and physical resources.

Manuscript received 9 March 2026; Revised 20 April 2026;; Accepted 15 June 2026; Available online 27 August 2026
DOI: https://doi.org/10.35882/ijeeemi.v8i3.335